

Using fluorescent beads to emulate single fluorophores

Luis A. Alemán-Castañeda,^{1,*} Sherry Yi-Ting Feng,² Rodrigo Gutiérrez-Cuevas,³
Isael Herrera,¹ Thomas G. Brown,² Sophie Brasselet,¹ Miguel A. Alonso^{1,2,**}

November 9, 2022

¹*Aix Marseille Univ, CNRS, Centrale Marseille, Institut Fresnel, Marseille 13013, France*

²*The Institute of Optics, University of Rochester, Rochester, NY 14627, USA*

³*Institut Langevin, ESPCI Paris, Université PSL, CNRS, 75005 Paris, France*

* *aleman-castaneda@fresnel.fr*; ** *miguel.alonso@fresnel.fr*

Abstract

In this work, we study the conditions under which fluorescent beads can be used to emulate single fluorescent molecules in the calibration of optical microscopes. Although beads are widely used due to their brightness and easy manipulation, there can be notable differences between the point spread functions (PSFs) they produce and those for single-molecule fluorophores, caused by their different emission pattern and their size. We study theoretically these differences for various scenarios, e.g. with or without polarization channel splitting, to determine the conditions under which the use of beads as a model for single molecules is valid. We also propose methods to model the blurring due to the size difference and compensate for it to produce PSFs that are more similar to those for single molecules.

1 Introduction

Fluorescence microscopy is a widely used technique for bio-imaging applications, not only due to its intrinsic optical contrast and/or specificity [1] but also for its compatibility with super-resolution techniques [2–4]. For example, single-molecule localization microscopy (SMLM) can achieve a spatial resolution of up to a few nanometers [4–7]. Additionally, when combined with polarization measurements, fluorescence microscopy can offer information about the sample’s structural properties, in particular, the average orientation and the order/wobbling of the molecules, both on the ensemble and the single-molecule regimes [8]. This information is key not only for biological applications but also in a broader sense, since not considering the fluorophore’s orientation can bias localization measurements [9, 10]. The simultaneous estimation of the emitters’ 3D localization and 3D orientation behavior is called single-molecule orientation localization microscopy (SMOLM). Common SMOLM techniques include polarization channel splitting [11–13] and point-spread function (PSF) engineering [14–19].

Fluorescence from a single molecule can be modeled as dipolar radiation [8, 20], resulting in a pattern at the pupil plane (or far field) that is not uniform in intensity nor in polarization, and it is strongly dependent on the dipole’s 3D orientation [21]. The resulting point spread function (PSF) at the detector plane can be predicted from this distribution. However, microscopes are typically imperfect optical systems that have optical aberrations and/or polarization distortions that bias both localization and orientation estimations. Furthermore, these distortions may change across the field of view. Therefore, it is important to characterize the imaging system properly, and one way to do so is by imaging fluorescent beads, given their brightness (significantly larger than that of single fluorophores) and easy manipulation [22–27].

There are two main differences, however, between the PSFs for beads and those for actual single molecule emitters. First, while beads can be quite small (a few tens of nanometers), they are still much larger than single molecules and this spatial extension induces a blurring effect on the measured PSF. Second, beads are composed of many fluorophores with different orientations [22, 23], making their emission pattern quite different from that of a single dipole: the light emitted by a bead is in principle unpolarized and therefore fills fairly uniformly the pupil of the system, in contrast to single-molecule fluorophores that have specific polarization and intensity distributions.

In this paper, we study the circumstances under which fluorescent beads, with the help of polarizers or other optical components at the pupil plane, can be used to produce PSFs that mimic those for single fluorophores with different orientations. We start by discussing the emission of a fixed dipole and that of an unpolarized point-like emitter. We then study the effect of bead size, both through numeric and semi-analytic approaches. We consider

two simple models for the bead emission. In particular, the semi-analytic approach offers a series of corrections that can be used to counter the bead size effects on the PSF in image post-processing. The analysis presented here follows directly from several theoretical advances due to Prof. Emil Wolf, such as the Richards-Wolf method for modeling high numerical aperture systems [28] and the theory for partial spatial coherence and polarization [29], so we think this work is appropriate for this special issue celebrating his hundredth birthday.

2 Radiation from a fixed dipole

In this section we describe the forward model based on the Richards-Wolf formalism [16, 28, 30] used to calculate the PSF of a single dipole at a longitudinal distance z from focus and whose orientation is fixed and aligned with the unit vector $\hat{\boldsymbol{\mu}}^T = (\mu_x, \mu_y, \mu_z)$. We ignore for now transverse (x, y) displacements, since they correspond simply to a linear phase factor at the pupil plane, and in turn to a transverse displacement at the detector plane. Let us denote as $\mathbf{E}_p(\mathbf{u})$ the field at the system's pupil plane, where \mathbf{u} is a dimensionless pupil position with polar coordinates (u, φ) , normalized so that the edge of the pupil corresponds to $u = \text{NA}$, the numerical aperture of the objective. Hence the field at the pupil plane can be approximated by

$$\mathbf{E}_p(\mathbf{u}; z, d) = e^{-iknz\gamma(u)} e^{-knd \text{Im}\{\gamma(u)\}} \mathbb{K}(\mathbf{u}) \cdot \hat{\boldsymbol{\mu}} \quad (1)$$

where d is the distance from the nominal focus to the coverslip, $\text{Im}\{\}$ the imaginary part, n the refractive index of the medium embedding the fluorophore, and for an aplanatic system $\gamma(u) = \sqrt{1 - (u/n)^2}$ [28]. Here, $\mathbb{K}(\mathbf{u})$ is a 2×3 matrix that determines the amplitude/polarization distribution at the pupil plane (where the field is paraxial and hence requires only two components) generated by each of the three Cartesian components of the dipole source, according to

$$\mathbb{K}(\mathbf{u}) = \begin{pmatrix} g_0(u) + g_2(u) \cos 2\varphi & g_2(u) \sin 2\varphi & g_1(u) \cos \varphi \\ g_2(u) \sin 2\varphi & g_0(u) - g_2(u) \cos 2\varphi & g_1(u) \sin \varphi \end{pmatrix}, \quad (2)$$

where

$$g_{0,2}(u) = \frac{t_p(u)\gamma(u) \pm t_s(u)}{2\sqrt{\gamma(nu/n')}}}, \quad (3a)$$

$$g_1(u) = \frac{u}{n} \frac{t_p(u)}{\sqrt{\gamma(nu/n')}}} \quad (3b)$$

with $t_p(u)$ and $t_s(u)$ being the transmission coefficients for the radial (transverse-magnetic) and azimuthal (transverse-electric) components of the field, respectively, and n' is the refractive index of the immersion oil (which is assumed to have the same index as the coverslip).

Figure 1 shows the intensity distribution for a horizontal dipole embedded either in water (a,b) or in air (c), and at different distances from the coverslip. Notice that we observe supercritical angle fluorescence (SAF) if the NA of the system is larger than the refractive index of the embedding medium. The strength of SAF depends strongly on the distance between the dipole and the coverslip, $d - z$, being significant only for $(d - z) < \lambda$. Figure 2 shows the polarization distribution at the pupil for three orthogonal dipole orientations in air. Polarization within the pupil is everywhere linearly polarized except in the annular region occupied by SAF (outside the red circle), in which t_p and t_s become complex and introduce a relative phase between the radial and azimuthal field components. For a longitudinal dipole, however, polarization remains linear even in the SAF region since only the radial component contributes. Note that for transverse dipoles, polarization at the pupil is largely in the dipole direction for low NA, but less so for higher NA.

The field from the pupil is focused on the detector, which in the ideal case corresponds to a Fourier transform of the form

$$\mathbf{E}_{\text{det}}(\bar{\boldsymbol{\rho}}; z) = \frac{f}{M^2\lambda} \int \mathbb{J}(\mathbf{u}) \cdot \mathbf{E}_p(\mathbf{u}; z) \exp\left(-ik\mathbf{u} \cdot \frac{\bar{\boldsymbol{\rho}}}{M}\right) d^2\mathbf{u}, \quad (4)$$

where M is the optical system's magnification, f is the focal length of the focusing system, and $\bar{\boldsymbol{\rho}}$ is the position variable at the detector. We employ barred variables to distinguish the detector coordinates from the object space of the fluorophores. Here, $\mathbb{J}(\mathbf{u})$ represents a Jones matrix describing any manipulation on the field performed after the pupil plane, ranging from a simple uniform analyzer before the detector to a more complex birefringent mask, like those used in many PSF engineering techniques [16, 18, 19, 25–27]. In what follows we use the shorthand \mathcal{F} for this Fourier transform including the corresponding physical parameters. The final intensity at the detector is given by

$$I_{\text{det}}(\bar{\boldsymbol{\rho}}; z) = \left[\mathcal{F} \left\{ \mathbb{J}(\mathbf{u}) \cdot \mathbf{E}_p(\mathbf{u}) \right\} \right]^\dagger \left[\mathcal{F} \left\{ \mathbb{J}(\mathbf{u}) \cdot \mathbf{E}_p(\mathbf{u}) \right\} \right], \quad (5)$$

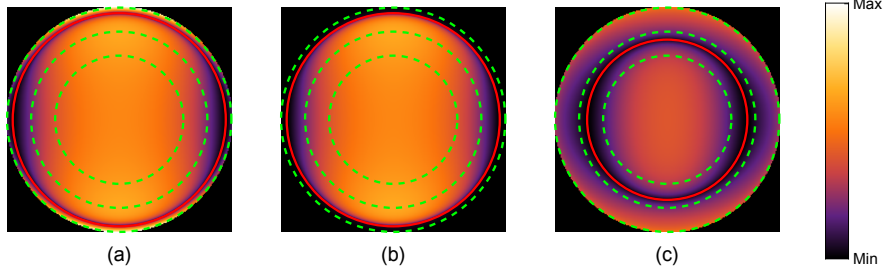


Figure 1: Intensity distribution at the pupil generated by a horizontal dipole embedded in (a,b) water, and (c) air. The dashed green circles denote (from smaller to larger) $\text{NA} = 0.8, 1.1$ and 1.4 , while the red circle indicates $\text{NA} = n$, which is the radial lower bound of the annular region corresponding to SAF. In (a) and (c) SAF is important since the dipole is close to the coverslip, $(d - z) = \lambda/5$, while in (b) SAF is negligible since the dipole is further away, $(d - z) = \lambda$.

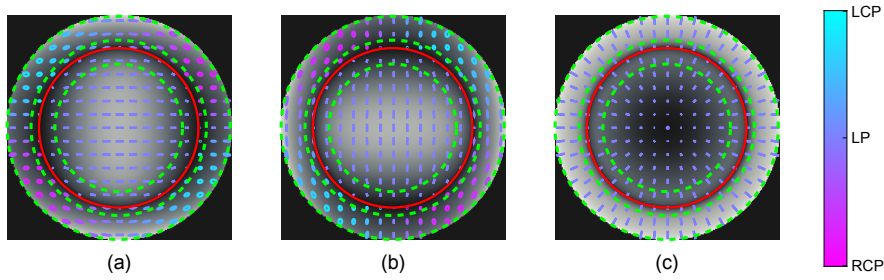


Figure 2: Polarization distribution at the pupil generated by a (a) transverse horizontal, (b) transverse vertical, and (c) longitudinal dipole. Polarization ellipses are plotted on top of the respective intensity distributions, with cyan denoting left-handedness and magenta right-handedness. The dashed green circles denote (from smaller to larger) $\text{NA} = 0.8, 1.1$ and 1.4 , while the red circle indicates $\text{NA} = n$, where SAF begins.

where \dagger denotes transpose conjugation.

Now we proceed to expand in a Taylor series in z the intensity at the detector plane. This expansion will let us not only gain physical insight but also compare more realistically different sources such as fixed dipoles, unpolarized point-like emitters, and fluorescent beads. It will also be the basis for a semi-analytic model for accounting for bead size discussed in Section 4. Let this Taylor expansion be centered around some value z_0 :

$$I_{\text{det}}(\bar{\rho}; z) = \sum_{m=0}^{\infty} \frac{1}{m!} (z - z_0)^m \frac{\partial^m I_{\text{det}}}{\partial z^m}(\bar{\rho}; z_0) = \sum_{m=0}^{\infty} \frac{1}{m!} (z - z_0)^m \mathcal{I}_m(\bar{\rho}; z_0), \quad (6)$$

where in the last step we introduced the notation $\mathcal{I}_m(\bar{\rho}; z_0)$ for the m th derivative in z of the intensity. While written here as a sum over all non-negative integers, in practice the sum in m will be truncated at some modest value. Since the only dependence in z of the field \mathbf{E}_{det} is within the complex phase factor, we have

$$\frac{\partial^m \mathbf{E}_{\text{det}}}{\partial z^m}(\bar{\rho}; z) = \mathcal{F} \{ \mathbb{J}(\mathbf{u}) \cdot \mathbf{E}_p(\mathbf{u}; z) [-ikn\gamma(u)]^m \}, \quad (7)$$

so that the coefficients of the series become

$$\mathcal{I}_m(\bar{\rho}; z_0) = \sum_{l=0}^m \frac{m!}{l! (m-l)!} \mathcal{F} \{ \mathbb{J}(\mathbf{u}) \cdot \mathbf{E}_p(\mathbf{u}; z_0) [-ikn\gamma(u)]^l \}^\dagger \times \mathcal{F} \{ \mathbb{J}(\mathbf{u}) \cdot \mathbf{E}_p(\mathbf{u}; z_0) [-ikn\gamma(u)]^{m-l} \}. \quad (8)$$

In general, \mathcal{I}_m for $m > 0$, are not intensities but rather changes in the intensity with z , so they can be positive and negative. Figure 3 shows the distribution of \mathcal{I}_m at the nominal focal distance for different constant choices for the Jones matrix \mathbb{J} , namely the identity (no manipulation before focusing), and pairs of orthogonal polarization projections before the detector: horizontal-vertical and circular left-right. Note that the PSF is slightly elongated in the dipole direction (horizontally). Given the absence of SAF contributions and aberrations, the focused field is

symmetric around the nominal image plane, so that the odd derivative terms vanish in Fig. 3(a-c). Nevertheless, as shown in Fig. 3(d,e) when a circular analyzer is used, the first derivative does not vanish, hence breaking the symmetry. That is, given the contribution of \mathcal{I}_1 , the circularly polarized PSFs counter-rotate with respect to each other with defocus, as shown in Fig. 4. This could serve as the basis of a SMOLM technique for the estimation of transverse dipoles' localization and orientation, consisting of forming separately the PSF of each circular component: for perfectly in-focus dipoles the elongation reports on the dipole direction, while for defocused dipoles the amount of counter-rotation between the PSFs reports on the defocus. This behavior is reminiscent of that of the PSFs in a technique proposed recently [16]. However, the signature of the elongation and rotation of the PSFs in Fig. 4 may not be sufficiently strong to remain detectable in the presence of noise and camera pixelation.

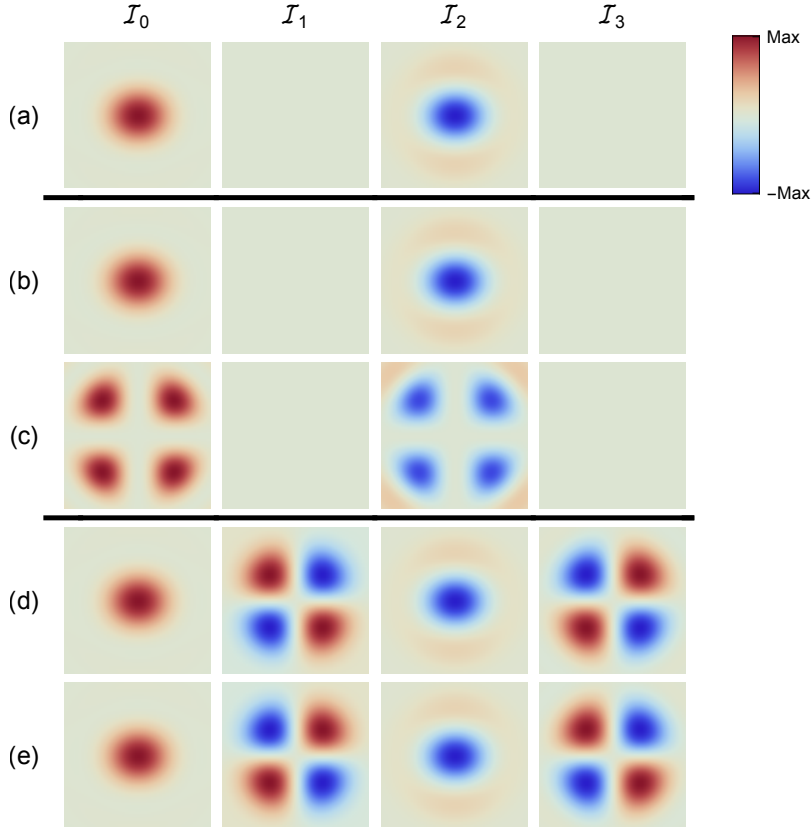


Figure 3: PSFs \mathcal{I}_0 and subsequent Taylor components \mathcal{I}_m for a system with NA= 1.3 (no SAF) imaging a horizontal dipole in water ($n \approx 1.33$), for several polarization projections following the pupil: (a) no polarizer, (b) horizontal, (c) vertical, (d) left-circular and (e) right-circular polarizers. The elements of each column are normalized to the largest value in the column, but the results in (c) are scaled by a factor of 128 and those in (d) and (e) are scaled by a factor of 2. Here $\lambda = 525\text{nm}$ and squares are of the length of $1\mu\text{m}$ on the object side.

3 Radiation from an unpolarized emitter.

An unpolarized (in the 3D sense) point-like emitter can be understood as the incoherent sum of the contributions from three orthogonal dipoles of equal magnitude. Without loss of generality, we can use three dipoles aligned with the coordinate axes x (transverse horizontal), y (transverse vertical), and z (longitudinal). Therefore, the intensity distribution at the pupil can be written as

$$I_{\text{pupil,unp}} = |\mathbb{K} \cdot \hat{\mathbf{x}}|^2 + |\mathbb{K} \cdot \hat{\mathbf{y}}|^2 + |\mathbb{K} \cdot \hat{\mathbf{z}}|^2 = \text{Tr} \{ \mathbb{K}^\dagger \mathbb{K} \}, \quad (9)$$

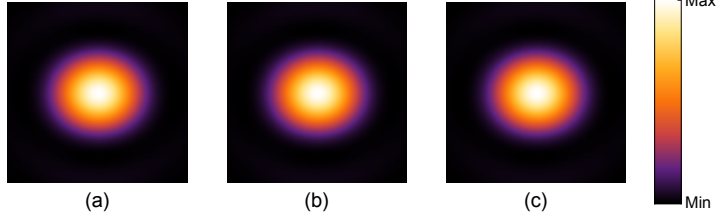


Figure 4: Simulated PSFs for an horizontal dipole at $z = \lambda/3$ embedded in water, i.e. $n \approx 1.33$ and $\text{NA} = 1.3$, (a) without any polarization projection, and for the (b) left-circular and (c) right-circular components. Note the counter-rotation in (b) and (c). Here $\lambda = 525\text{nm}$ and squares are of the length of $1\mu\text{m}$ on the object side.

where $\hat{\mathbf{x}}$, $\hat{\mathbf{y}}$ and $\hat{\mathbf{z}}$ are 3D unit vectors in these three directions, and $\text{Tr}\{\}$ denotes the trace. It can be shown that this intensity distribution reduces to the radially symmetric function

$$I_{\text{pupil,unp}}(u) = \frac{|t_p(u)|^2 + |t_s(u)|^2}{\gamma(u)} P(u; d), \quad (10)$$

where $P(u; d) = \exp[-2 \text{Im}\{kn(d-z)\gamma(u)\}]$ with $(d-z)$ being the distance to the coverslip and $\text{Im}\{\}$ denoting the imaginary part. Note that $P(u; d) = 1$ for $u \leq n$. Figure 5 shows this intensity distribution compared to the one of a horizontal dipole, as well as the resulting distribution after passing through a horizontal polarizer. Note that they are similar for low NA but less so for higher NA.

Additionally, the distribution of the normalized Stokes parameters over the pupil plane, i.e. $s_i(\mathbf{u}) = S_i(\mathbf{u})/S_0(\mathbf{u})$ for $i = 1, 2, 3$ where $S_0(\mathbf{u}) = I_{\text{pupil,unp}}(\mathbf{u})$, are found to be given by

$$s_1(\mathbf{u}) = \frac{|t_p(u)|^2 - |t_s(u)|^2}{|t_p(u)|^2 + |t_s(u)|^2} \cos 2\varphi, \quad (11a)$$

$$s_2(\mathbf{u}) = \frac{|t_p(u)|^2 - |t_s(u)|^2}{|t_p(u)|^2 + |t_s(u)|^2} \sin 2\varphi, \quad (11b)$$

$$s_3(\mathbf{u}) = 0, \quad (11c)$$

which (unlike $I_{\text{pupil,unp}}$) depend on φ although as a simple sinusoidal modulation. The degree of polarization is rotationally symmetric:

$$\text{DOP}(u) = \frac{||t_p(u)|^2 - |t_s(u)|^2|}{|t_p(u)|^2 + |t_s(u)|^2}. \quad (12)$$

That is, the field at the pupil plane is fully unpolarized ($\text{DOP} = 0$) only at the center, and as one approaches the border of the pupil the difference between the Fresnel transmission coefficients introduces more and more polarization. This polarization can be particularly strong for the SAF contribution. This is illustrated in Fig. 6, which shows the pupil distributions of the normalized Stokes parameters as well as the degree of polarization of an unpolarized emitter close to the coverslip.

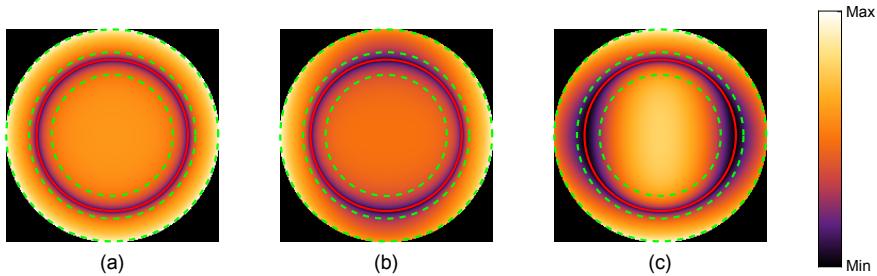


Figure 5: Intensity distributions at the pupil for (a) an unpolarized emitter, (b) an unpolarized emitter with a horizontal polarizer at the pupil, and (c) a horizontal dipole, all embedded in air, with a distance to the coverslip of $d = \lambda/5$, and for a system with $\text{NA} = 1.4$. The dashed green circles denote (from smaller to larger) $\text{NA} = 0.8, 1.1$ and 1.4 , while the red circle indicates the NA at which SAF begins.

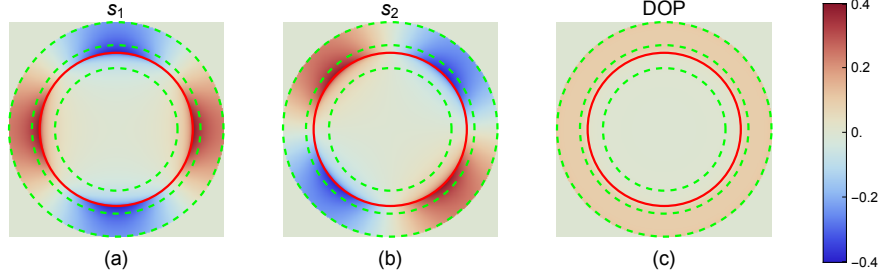


Figure 6: Normalized Stokes parameters (a) $s_{p,1}$ and (b) $s_{p,2}$, and (c) DOP_p , over the pupil for an unpolarized emitter embedded in air, with a distance to the coverslip of $d = \lambda/5$, and for a system with $NA= 1.4$. The dashed green circles denote (from smaller to larger) $NA = 0.8, 1.1$ and 1.4 , while the red circle indicates the NA at which SAF begins.

Like the pupil distributions, the PSFs can be constructed as the incoherent sum of the intensity contributions at the detector of the three orthogonal dipoles (horizontal, vertical, and longitudinal). Note that, given the linearity of the intensity, the Taylor expansion for the total intensity is simply the sum of the corresponding contributions $\mathcal{I}_m(\vec{\rho}; z_0)$ for each of these three orthogonal dipoles. Figure 7 shows the distribution of \mathcal{I}_m at the nominal focal distance for different constant choices for \mathbb{J} , namely the identity (no manipulation before focusing), and pairs of orthogonal polarization projections before the detector: horizontal-vertical and left-right circular. For horizontal and vertical polarization projections, the PSFs become elongated, whereas they retain rotational symmetry when no polarization projection takes place or for circular polarization projections. Note that, given the symmetry of the focused field around the nominal image plane in the absence of aberrations, the odd derivative terms vanish in Fig. 7.

4 Modeling the effects of bead size

As mentioned in the introduction, we can envision several simple models for the emission and geometry of a fluorescent bead, which include: (1) a *transparent solid sphere*, in which all points inside the bead emit light, and this light is able to emerge from the bead; (2) a *transparent shell*, in which only the points at the surface of the sphere emit, but the light from all these points is visible in any direction; (3) an *opaque shell*, where only the light from points at the surface in line of sight can be detected, perhaps following a Lambertian emission model. Given their transparency, fluorescent beads most likely are best described by the first model, particularly when their index is well matched to that of its surrounding medium. However, we also describe the second model in what follows, given how similar its mathematical description is to that of the first. The third model will not be discussed further, since it is harder to model and would be relevant, for example, if the refractive index of the bead had an important imaginary part. In what follows we use two approaches: (a) a stochastic one based on the incoherent superposition of contributions from randomly oriented dipoles with random positions following the desired geometry, and (b) a deterministic one that assumes the same emission at all points, which can be modeled either numerically or semi-analytically.

4.1 Stochastic approach

A real fluorescent bead can be simulated as a collection of n_s fluorophores that are randomly oriented (with directions uniformly distributed over a unit sphere) and which are randomly but uniformly distributed spatially following the desired geometry. Figure 11 shows the PSFs generated through the sum of $n_s = 1000$ fluorophores for both a transparent solid sphere and a shell, and compares them to the PSF of a point-like unpolarized emitter. Note that the difference between them is not perfectly rotationally symmetric, due to the finite sampling and the asymmetries in the random positions and directions used. Although time- and resource-consuming, stochastic approaches are flexible enough to simulate a wide variety of fluorophore distributions not limited to the interior or surface of a sphere. Nevertheless, this approach does not offer much physical insight, so we consider instead deterministic methods.

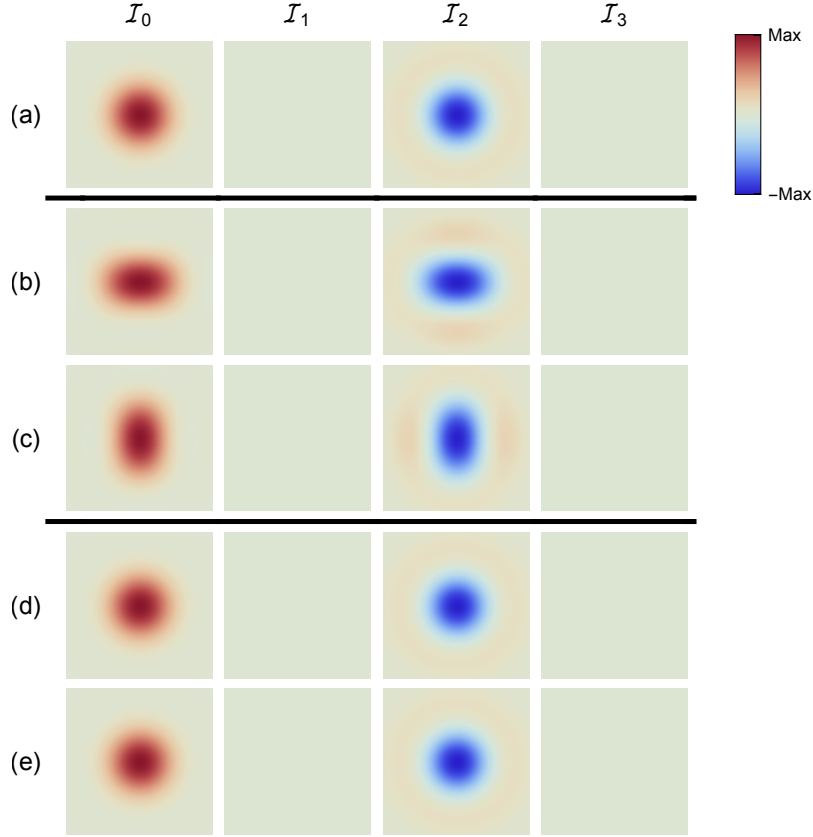


Figure 7: PSFs I_0 and subsequent Taylor components I_m for a system with NA= 1.3 imaging an unpolarized emitter in water ($n \approx 1.33$), for several polarization projections following the pupil: (a) no polarizer, (b) horizontal, (c) vertical, (d) left-circular and (e) right-circular polarizers. The elements of each column are normalized to the largest value in the column, but a factor of 2 is applied in rows (b-e) with respect to (a). Here $\lambda = 525\text{nm}$ and squares are of length of $1\mu\text{m}$ on the object side.

4.2 Deterministic approach: transparent solid sphere

Let us assume that the intensity distribution at the detector due to a source at (x, y, z) is $I_{\text{det}}(\bar{\rho}; x, y, z)$ (where again coordinates without a bar describe the space of the bead, and barred coordinates correspond to the detector plane). Consider a transparent fluorescent bead of radius R centered at (x_0, y_0, z_0) . The measured intensity can be calculated as a superposition of 2D convolutions:

$$I_{\text{tot}}(\bar{\rho}; x_0, y_0, z_0, R) = \sigma_V \int_{-R}^R I_{\text{det}}(\bar{\rho}; x_0, y_0, z_0 + z) * D(\bar{\rho}; R, z) dz, \quad (13)$$

where σ_V is the volumetric density of fluorophores, $*$ denotes a 2D convolution in the detector coordinates, and $D(\bar{\rho}; R, z)$ is a disk function representing the magnified section of the bead at z . For numerical purposes, the integral in z can be approximated through a discrete sum of N slices, i.e.

$$I_{\text{tot}}(\bar{\rho}; x_0, y_0, z_0, R) \approx \sigma_V \sum_{j=1}^N I_{\text{det}}(\bar{\rho}; x_0, y_0, z_0 + z_j) * D(\bar{\rho}; R, z_j) \Delta z, \quad (14)$$

where

$$\Delta z = \frac{2R}{N}, \quad z_j = \left(j - \frac{1}{2}\right) \Delta z - R. \quad (15)$$

This can be implemented as

$$I_{\text{tot}} = \sigma_V \mathcal{F}^{-1} \left\{ \sum_{j=1}^N \mathcal{F} \{ I_{\text{det}}(\bar{\rho}; x_0, y_0, z_0 + z_j) \} \mathcal{F} \{ D(\bar{\rho}; R, z_j) \} \right\} \Delta z, \quad (16)$$

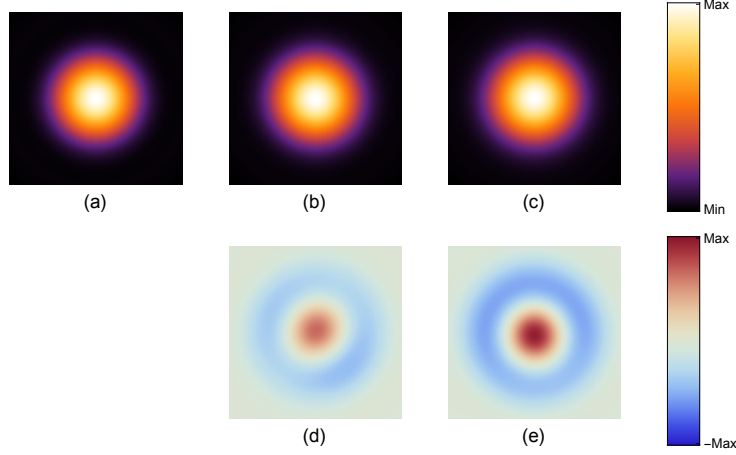


Figure 8: PSFs of (a) a point-like unpolarized emitter, and (b,c) a 200 nm diameter fluorescent bead modeled as (b) a transparent solid sphere and (c) a transparent shell. Here $NA = 1.3$ and embedding media is water ($n \approx 1.33$). For the stochastic simulations, 1000 random positions and orientations were used. The difference between the PSF of a point-like emitter and that of (d) a transparent solid sphere and (e) a transparent shell. The value range corresponds roughly to 7% of the maximum value of the recorded PSF. Squares are of the length of $1\mu\text{m}$ on the object side.

in which

$$\mathcal{F}\{D(\bar{\rho}; R, z_j)\}(u) = 2\pi M^2 R_j^2 \frac{J_1(kuR_j)}{kuR_j}, \quad (17)$$

where M is the system's transverse magnification and $R_j = \sqrt{R^2 - z_j^2}$, i.e. the section of the bead at z_j . Note that the way the sum is implemented, using $N = 1$ corresponds to a convolution of the PSF with a disk of the same nominal radius as the bead used, giving a very simple model for the blurring effect.

Alternatively, a semi-analytic approach can be used based on a Taylor expansion in z around z_0 of I_{det} like that in Eq. (6), namely,

$$I_{\text{tot}}(\bar{\rho}; x_0, y_0, z_0, R) = \sigma_V \sum_{m=0}^{\infty} \frac{1}{m!} \mathcal{I}_{\text{det},m}(\bar{\rho}; x_0, y_0, z_0) * G_m(\bar{\rho}; R), \quad (18)$$

where, for sufficiently small beads, a good approximation can be obtained by truncating the sum at a low value of m . The function $G_m(\bar{\rho}; R)$ is defined as the easily-solvable integral

$$G_m(\bar{\rho}; R) = \int_{-R}^R z^m D(\bar{\rho}; R, z) dz = \int_{-\ell/2}^{\ell/2} z^m dz = \begin{cases} \frac{1}{2^{m(m+1)}} \ell^{m+1}, & m \text{ even,} \\ 0, & m \text{ odd.} \end{cases} \quad (19)$$

where $\ell(\bar{\rho}; R)$ is the length in z of the bead at a given transverse position. In terms of the detector coordinates, this length is given by

$$\ell(\bar{\rho}; R) = 2\sqrt{R^2 - \left|\frac{\bar{\rho}}{M}\right|^2}, \quad (20)$$

where M is the system's transverse magnification. It follows that

$$I_{\text{tot}} = \sigma_V \mathcal{F}^{-1} \left\{ \sum_{m=0}^{\infty} \mathcal{F} \left\{ \frac{1}{m!} \mathcal{I}_{\text{det},m} \right\} \mathcal{F} \{G_m\} \right\} \quad (21)$$

where we dropped the arguments for brevity. Since G_m are radially symmetric functions, the Hankel transform can be used to obtain their Fourier transforms:

$$\mathcal{F}\{G_m\}(u) = 4\pi M^{m+2} R^{m+3} (m-1)!! \frac{j_{\frac{m}{2}+1}(kuR)}{(kuR)^{\frac{m}{2}+1}}, \quad (22)$$

where $n!! = (n)(n-2)\dots$ is the double factorial, and j_n denotes a spherical Bessel function of order n . Note that Eq. (22) is valid for even $m \geq -2$.

Figure 9 shows the PSFs for the particular case of a bead with diameter $2R = 200\text{nm}$ embedded in water, imaged by a system with $\text{NA} = 1.3$. These PSFs were obtained by using both deterministic models: (a) the discrete sum of convolutions in Eq. (14) with $N = 6$, (b) the same model but for $N = 1$, namely a simple convolution with a uniform disk, and (c,d) the semi-analytical approach in Eq. (21) with the sum truncated at (c) $m = 0$, namely a simple convolution with the apodized disk G_0 , and (d) $m = 2$, that is, including an extra correction. We take as ground truth the result shown in Fig. 9(a). The relative difference between this ground truth and the other results for a given NA is shown in Fig. 9(e-g). We see that, for large NAs the two models including only one contribution, namely the convolution with a uniform disk $D(\bar{\rho})$ (second column) and with an apodized disk $G_0(\bar{\rho})$ (third column), give results with similar levels of error, whereas the semi-analytic result including a second order correction gives an error 10 times smaller. Note that the errors in Fig. 9(e) and (f) have opposite behavior, due to the fact that $G_0(\bar{\rho})$ weights more heavily the center compared to the borders, while $D(\bar{\rho})$ is uniform.

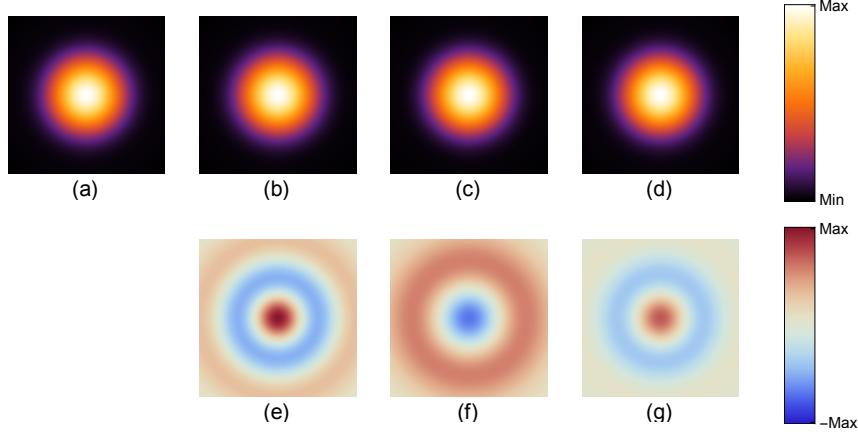


Figure 9: Simulated PSFs for a 200nm diameter fluorescent bead using: (a) numerical integration with 6 slices, (b) one slice, i.e. uniform disk model, (c) zeroth order semi-analytic model, and (d) second-order semi-analytic model. (e-g) Difference between the numerical integration result and each of the other models respectively. Note that (e) and (f) are normalized to 0.5% of the peak value of the PSF, whereas (g) is normalized to 0.05% of the maximum value recorded for (a). Note that this small error in (g) is not necessarily due entirely to the truncation at $m = 2$ of the series approach, but might also be due to errors in the estimate chosen as the ground truth. Here $\text{NA} = 1.3$, the embedding medium is water ($n \approx 1.33$) and squares are of the length of $1\mu\text{m}$ on the object side.

In order to fully compare the models, the RMS error for a range of NAs and bead radii was computed using again as ground truth the results of Eq. (14) with $N = 6$. Figure 10 shows the logarithm of the RMS error. Notice that for small NA the convolution with the apodized disk, $G_0(\bar{\rho})$, is much better than the convolution with a uniform disk, $D(\bar{\rho})$, but for larger NA they have similar performance, and the uniform disk even outperforms the apodized one. An interesting difference between these two simple models is that convolving with $G_0(\bar{\rho})$ leads to an estimate whose error grows with both NA and R , while convolving with $D(\bar{\rho})$ leads to an error that is roughly independent of NA. The semi-analytical model becomes again roughly independent of NA when the second order correction is included.

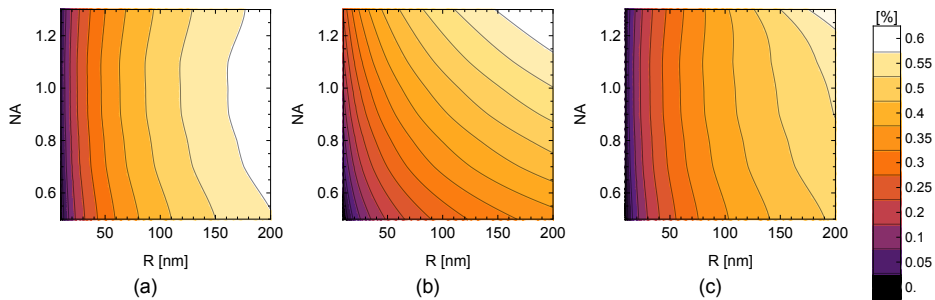


Figure 10: RMS error, for varying NA and bead radius, between the numerically integrated PSF and the PSFs obtained by using: (a) Eq. (14) with $N = 1$ (convolution with a flat disk), (b) Eq. (21) truncated at $m = 0$ (convolution with an apodized disk), and (c) Eq. (21) truncated at $m = 2$. Here $\text{NA} = 1.3$ and the embedding medium is water ($n \approx 1.33$).

A key result, particularly for small NA systems, is that the zero-order correction,

$$\mathcal{F}\{G_0\}(u) = 4\pi M^2 R^3 \frac{j_1(kuR)}{(kuR)}, \quad (23)$$

can be used to directly deconvolve the measured intensity at the detector to obtain a more realistic PSF, i.e.

$$I' = \mathcal{F}^{-1} \left\{ \frac{\mathcal{F}\{I_{\text{measured}}\}}{\mathcal{F}\{G_0\}} \right\}. \quad (24)$$

This deconvolution is reliable under appropriate signal-to-noise ratio conditions, and requires that the zeros of $\mathcal{F}\{G_0\}$ lie well outside the incoherent pupil radius of 2NA . The first zero of $\mathcal{F}\{G_0\}$ is at $u' \approx 1.43\pi/(kR)$, giving the safety condition for the bead's diameter $2R < 0.715\lambda/\text{NA}$. On the other hand, for larger NA systems if the uniform disk model were to be used, a similar condition could be obtained based on the first zero of $\mathcal{F}\{D\}$ that would be slightly more restrictive: $2R < 0.61\lambda/\text{NA}$.

4.3 Deterministic approach: transparent shell

Although we do not expect this model to be a faithful representation of a fluorescent bead, we include it given its simplicity, and in case it can be useful in a different application. Following the same procedure as in the previous section, let us now assume a fluorescent empty shell of radius R centered at (x_0, y_0, z_0) . Again, the measured intensity can be calculated as a superposition of 2D convolutions:

$$I_{\text{tot}}(\bar{\rho}; x_0, y_0, z_0, R) = \sigma_S \int_{-R}^R I_{\text{det}}(\bar{\rho}; x_0, y_0, z_0 + z) * A(\bar{\rho}; R, z) dz, \quad (25)$$

where σ_S is the surface density of fluorophores, $A(\bar{\rho}; R, z)$ is an impulse ring function representing the magnified perimeter of the sphere at z . Numerically, this integral in z can be computed through a discrete sum of N slices as

$$I_{\text{tot}} = \sigma_S \mathcal{F}^{-1} \left\{ \sum_{j=1}^N \mathcal{F}\{I_{\text{det}}(\bar{\rho}; x_0, y_0, z_0 + z_j)\} \mathcal{F}\{A(\bar{\rho}; R, z_j)\} \right\} \Delta z, \quad (26)$$

where Δz and z_j are defined as in Eq. (15) and

$$\mathcal{F}\{A(\bar{\rho}; R, z_j)\}(u) = \mathcal{F}\{\delta(\rho - MR_j)\}(u) = 2\pi MR_j J_0(kuR_j), \quad (27)$$

in which once more $R_j = \sqrt{R^2 - z_j^2}$, i.e. it is the radius of the bead at z_j .

On the other hand, as in the previous section, a semi-analytic approach can be used based on a Taylor expansion in z around z_0 of I_{det} , namely,

$$I_{\text{tot}}(\bar{\rho}; x_0, y_0, z_0, R) = \sigma_S \sum_{m=0}^{\infty} \frac{1}{m!} \mathcal{I}_{\text{det},m}(\bar{\rho}; x_0, y_0, z_0) * H_m(\bar{\rho}; R), \quad (28)$$

Where the function $H_m(\bar{\rho}; R)$ is defined as the easily-solvable integral

$$H_m(\bar{\rho}; R) = \int_{-R}^R z^m A(\bar{\rho}; R, z) dz = \int_{-R}^R z^m \frac{\delta(z - \ell/2) + \delta(z + \ell/2)}{|z|/R} dz, \quad (29)$$

where ℓ is defined as in Eq. (20), and which ultimately leads to

$$H_m(\bar{\rho}; R) = \begin{cases} R \frac{\ell^{m-1}}{2^{m-2}}, & m \text{ even,} \\ 0, & m \text{ odd.} \end{cases} \quad (30)$$

Note that in general $H_m = R(m-1)G_{m-2}$ from the previous section and so the total intensity can be expressed as

$$I_{\text{tot}} = \sigma_S \mathcal{F}^{-1} \left\{ \sum_{m=0}^{\infty} \mathcal{F} \left\{ \frac{1}{m!} \mathcal{I}_{\text{det},m} \right\} \mathcal{F}\{G_{m-2}\} \right\}, \quad (31)$$

in which $\mathcal{F}\{G_{m-2}\}$ is given in Eq. (22).

5 Mimicking transverse dipoles with beads

We now evaluate how well a fluorescent bead supplemented with a polarizer at the pupil can be used to mimic the PSF of a transverse point dipole. The intensity distribution of a transverse dipole in the pupil is fairly uniform except at the pupil edge and is similar to an unpolarized emitter. Therefore, by inserting a linear polarizer at the pupil, one can make the PSF of an unpolarized emitter mimic the one for a transverse dipole [16, 24]. For systems with small NA, this should be a good approximation, while for higher NAs differences become more evident at the edge of the pupil distribution, both in intensity and polarization, causing discrepancies between the corresponding PSFs. In this section we first study how a point-like emitter can mimic a real transversal dipole, and then we incorporate the effects of bead size using the results of the previous section. Particularly we highlight how the proposed G_0 function can be used to deconvolve the measured PSFs to correct the blurring introduced by the bead size.

5.1 Mimicking transverse dipoles using a point-like source

Let us, without loss of generality, consider a horizontal dipole (aligned with the x axis). The Jones matrix at the pupil is then written as

$$\mathbb{J}(\mathbf{u}) = \mathbb{J}'(\mathbf{u})\mathbb{P}_x, \quad (32)$$

where $\mathbb{P}_x = \hat{\boldsymbol{\rho}}_x \hat{\boldsymbol{\rho}}_x^\dagger$ is a horizontal projection matrix representing a horizontal polarizer, with $\hat{\boldsymbol{\rho}}_x$ being a 2D unit vector in the horizontal direction. That is, the Jones matrix representing all the manipulations after the pupil can be chosen to represent the cascade of a horizontal linear polarizer and other possible manipulations represented by the Jones matrix $\mathbb{J}'(\mathbf{u})$. Let us for now set this second Jones matrix to the identity. It can be shown that the intensity distribution at the pupil just after the polarizer becomes

$$I_{p,\text{mimic}}(\mathbf{u}) = \left(g_0^2(u) + g_2^2(u) + 2g_0(u)g_2(u) \cos 2\varphi + g_1^2(u) \cos^2 \varphi \right) P(u; d), \quad (33)$$

whose only difference with that for a true horizontal dipole is the last term, $g_1^2(u) \cos^2 \varphi$, meaning that the difference is zero only at central axial line perpendicular to the polarization.

Perhaps of more consequence to the final PSFs are the differences in spatial coherence and polarization over the pupil. For a pure horizontal dipole source, the cross-spectral density matrix is

$$\mathbb{W}_x(\mathbf{u}_1, \mathbf{u}_2) = \mathbb{K}(\mathbf{u}_1) \hat{\mathbf{x}} \hat{\mathbf{x}}^\dagger \mathbb{K}^\dagger(\mathbf{u}_2), \quad (34)$$

where $\hat{\mathbf{x}} \hat{\mathbf{x}}^\dagger$ is a 3D projection in the x direction (as opposed to \mathbb{P}_x which enacts a 2D projection). Note that \mathbb{W}_x is simply the outer product of $\mathbb{K} \hat{\mathbf{x}}$ and its conjugate (each evaluated at a different pupil point), so there is no statistical decorrelation between any two pupil points. This is not the case, on the other hand, for the mimicked dipole based on an unpolarized emitter and a polarizer at the pupil. As shown in Fig. 2, all three orthogonal dipole directions contribute to the x component at the pupil, each with a different distribution (two of them being important mainly at the edges of the pupil). These contributions are mutually incoherent. Therefore, the cross-spectral density matrix at the pupil right after the polarizer due to an unpolarized emitter at the nominal source plane is given by

$$\mathbb{W}_{p,\text{mimic}}(\mathbf{u}_1, \mathbf{u}_2) = \mathbb{P}_x \mathbb{K}(\mathbf{u}_1) \mathbb{K}^\dagger(\mathbf{u}_2) \mathbb{P}_x \quad (35)$$

whose only nonzero element is the xx one. The degree of coherence for this nonzero component is then

$$\mu_{p,\text{mimic}}(\mathbf{u}_1, \mathbf{u}_2) = \frac{\{\mathbb{W}_{p,\text{mimic}}(\mathbf{u}_1, \mathbf{u}_2)\}_{xx}}{\sqrt{\{\mathbb{W}_{p,\text{mimic}}(\mathbf{u}_1, \mathbf{u}_1)\}_{xx} \{\mathbb{W}_{p,\text{mimic}}(\mathbf{u}_2, \mathbf{u}_2)\}_{xx}}}. \quad (36)$$

Note that for an emitter at the origin and in the absence of aberrations, this degree of polarization is real. Because $\{\mathbb{W}_{p,\text{mimic}}\}_{xx}$ is not a separable function of \mathbf{u}_1 and \mathbf{u}_2 , $\mu_{p,\text{mimic}}$ typically differs from unity for $\mathbf{u}_1 \neq \mathbf{u}_2$. This is illustrated in Fig. 11 for different slices of the pupil: two in which $\mathbf{u}_1 \parallel \mathbf{u}_2$, and one in which $\mathbf{u}_1 \perp \mathbf{u}_2$. Note in particular that for sufficiently separated points along the horizontal line, the degree of coherence vanishes and then becomes negative, due to the predominance at those points of the radially polarized contribution introduced by the longitudinal dipole. On the other hand, for any two pupil points along a vertical line ($\varphi_1 = \varphi_2 = \pi/2$), the polarizer eliminates the contributions from the vertical and longitudinal components, so that $\mu_{p,\text{mimic}} = 1$. Note that, in general, if both points are near the center of the pupil, the correlation approaches unity.

A quantitative measure of the similarity of both pupil distributions that accounts for amplitude, coherence and polarization is given by the following normalized projection:

$$C(\text{NA}) = \left\{ \frac{\iint \text{Tr}[\mathbb{W}_x(\mathbf{u}_1, \mathbf{u}_2) \mathbb{W}_{p,\text{mimic}}(\mathbf{u}_2, \mathbf{u}_1)] d^2\mathbf{u}_1 d^2\mathbf{u}_2}{\int \text{Tr}[\mathbb{W}_x(\mathbf{u}, \mathbf{u})] d^2\mathbf{u} \int \text{Tr}[\mathbb{W}_{p,\text{mimic}}(\mathbf{u}, \mathbf{u})] d^2\mathbf{u}} \right\}^{1/2}. \quad (37)$$

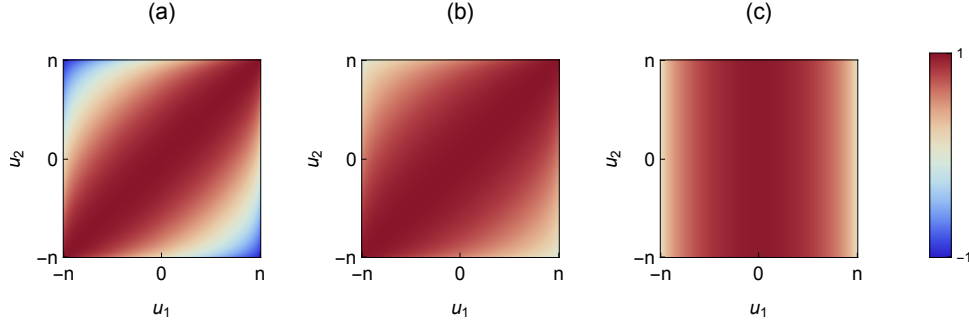


Figure 11: Degree of coherence $\mu_{p,mimic}$ for (a) $\varphi_1 = \varphi_2 = 0$, (b) $\varphi_1 = \varphi_2 = \pi/4$ and (c) $\varphi_1 = 0$ and $\varphi_2 = \pi/2$. Here the unpolarized emitter is assumed to be in the water, i.e. $n \approx 1.33$, and we only show $u_{1,2}$ within the non-SAF regions, since for SAF the degree of coherence becomes complex.

This measure achieves its maximum value of unity only if the two cross-spectral density matrices are identical. Given Parseval's identity, this measure also quantifies the difference in amplitude, coherence and polarization of the corresponding fields at the detector plane; given appropriate normalization, such RMS difference is given by $\sqrt{1 - C^2}$. However, the main interest in this work is in differences in PSF, namely only in intensity. Therefore, it is expected that $\sqrt{1 - C^2}$ will overestimate (and hence provide an upper bound for) the RMS errors in PSF.

It is convenient to use polar coordinates to evaluate this measure, and for the case considered here the integrals in the angular variables turn out to be solvable in closed form, leading to the expression

$$C(\text{NA}) = \frac{\mathcal{G}_0 + \mathcal{G}_2}{\sqrt{(\mathcal{G}_0 + \mathcal{G}_2)(\mathcal{G}_0 + \mathcal{G}_1/2 + \mathcal{G}_2)}}, \quad (38)$$

where $\mathcal{G}_j = \int |g_j(u)|^2 P(u; d) u du$.

So far we have considered the similarity of the PSFs for a transverse dipole and an unpolarized source (supplemented with a polarizer), both at the focal plane. Let us consider now the effect of a small amount of defocus. The Taylor expansion approach is useful for these purposes. Figure 7(b) shows the distribution of \mathcal{I}_m at the nominal focal distance for an unpolarized emitter followed by a horizontal polarizer. Given their uniform polarization, these PSF components maintain their distributions (except for a scaling factor) when projected onto any other polarization. Therefore, unlike a single horizontal dipole, as shown in Fig. 3(d,e), \mathcal{I}_m remains zero for odd m even when projecting onto a circular polarization, showing that the behavior of a transverse dipole under defocus is not being fully mimicked.

5.2 Mimicking transverse dipoles using finite-size beads

Let us finish by comparing the PSF of a true horizontal dipole to that of a mimicked one using a fluorescent bead and a linear polarizer at the pupil plane of the imaging system. For the latter, we use the approximation in Eq. (14) with $N = 7$. We also test the deconvolution method discussed in the previous section to compensate for the blurring introduced by the bead's size. Figure 12 shows the resulting simulated PSFs for a high NA system with no SAF ($\text{NA} < n$) for two cases: a standard imaging system with no aberrations, and a PSF engineering technique called CHIDO [16] based on a spatially-varying birefringent mask and circular polarization filtering.

We also computed the RMS error between the PSFs of an emulated fluorophore (with and without deconvolution) and a true horizontal dipole using different bead radii and various values of NA; these are shown in Fig. 13. Naturally, the error between the raw PSFs increases with both NA and bead radius, as shown in Fig. 13(a). Note from Fig. 13(b), though, that the deconvolution using the apodized disk G_0 eliminates almost completely the error's dependence on the radius (since the contours are essentially horizontal). Surprisingly, on the other hand, the deconvolution with a uniform disk, shown in Fig. 13(c) also accounts well for the size mismatch, and can give an error that is smaller for larger beads. We performed the same computations for CHIDO's engineered PSFs and obtained almost identical behavior, only with slightly higher RMS errors (approximately shifted up by 1%).

The reason why the effect of particle size is not necessarily negative can be understood from the coherence analysis. Due to the van Cittert-Zernike theorem, the effect of the spatial extension of the bead is to include an extra factor in the cross-spectral density matrix at the pupil given in Eq. (35). This factor turns out to take a simple analytic form for the two bead models discussed here: for the solid sphere it is given by $3\sigma_V j_1(\eta)/\eta$, while for

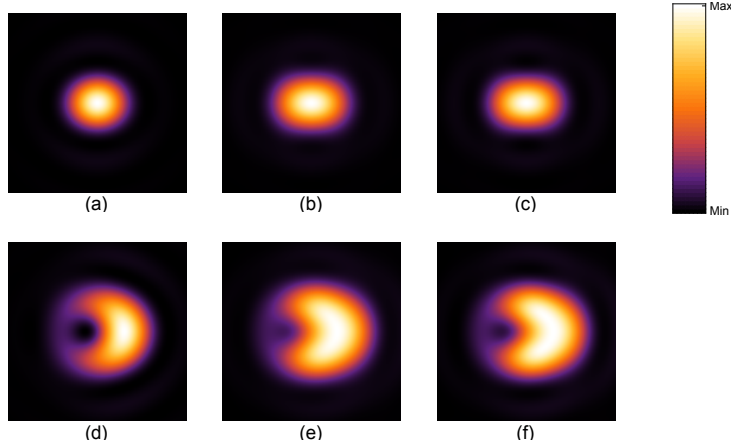


Figure 12: Simulation of the PSFs of (a,d) true horizontal dipoles, (b,e) mimicked ones using a 200nm diameter fluorescent bead and a polarizer, and (c,f) the deconvolution of the results in (b) and (e) with an apodized disk G_0 . These PSFs are (a-c) for a classical imaging system, and (d-f) for an engineered PSF [16]. Here $NA = 1.3$ and the embedding medium is water ($n \approx 1.33$). Squares represent $1.5\mu\text{m}$ in the object space.

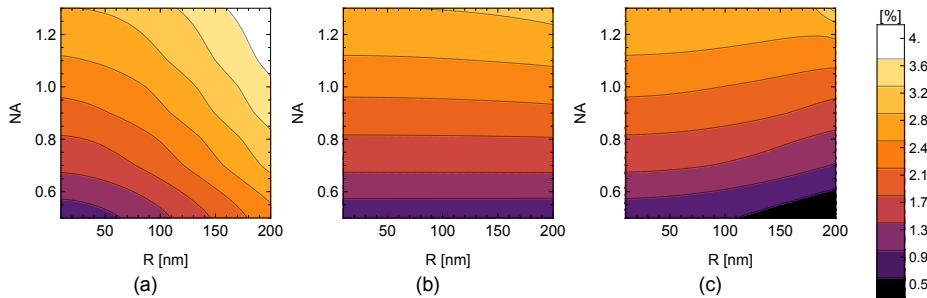


Figure 13: RMS error, for varying NA and bead radius, between the PSF of a true transverse dipole and the mimicked one using a fluorescent bead for: (a) no treatment, (b) deconvolution with the apodized disc G_0 , and (c) deconvolution with a uniform disk. Here $NA = 1.3$ and the embedding medium is water ($n \approx 1.33$).

the empty shell it is given by $\sigma_S \text{sinc}(\eta)$, where

$$\eta(\mathbf{u}_1, \mathbf{u}_2) = knR \sqrt{u_1^2 + u_2^2 - 2u_1u_2 \cos(\varphi_2 - \varphi_1) + [\gamma^*(u_1) - \gamma(u_2)]^2}. \quad (39)$$

Note that for $R \rightarrow 0$ the two factors tend to a constant equal to σ_V or σ_S . For $R > 0$, on the other hand, these factors decrease as u_1 and u_2 increase, meaning that the contributions from the edges of the pupil are partially suppressed. These are precisely the regions where the radiation pattern of a transverse dipole differs most from that of an unpolarized source supplemented with a linear polarizer, and therefore this suppression is not necessarily detrimental to the fit. As shown by the results shown in Fig. 13(c), increasing the radius can even lead to possibly better matches, particularly after post-processing of the PSFs.

6 Conclusions

In this work we studied how and under which conditions fluorescent beads can be used to mimic transverse dipoles. Specifically, we studied how the difference in emission pattern and size affect the measured PSFs. We proposed a semi-analytical method to model the effects of the bead size with different orders of corrections. These corrections correspond to a series of 2D convolutions which are less resource-consuming than a true 3D convolution. Additionally, we showed that the difference in size between a single fluorophore (which is essentially point-like for the purposes of optical modeling) and a fluorescent bead can be corrected satisfactorily by 2D deconvolution with the apodized disk function given in Eq. (19), hence reducing drastically the computational resources needed for post-processing. The blurring effect introduced by the finite size of the bead, however, can even be at times beneficial and lead to better matches after this post-processing of the PSFs.

The current manuscript focuses mostly on transverse dipoles, but future work will focus on extending this study to ways of emulating longitudinal and/or oblique dipoles by using beads and appropriate polarization plates.

References

- [1] J. Mertz, “Nonlinear microscopy: new techniques and applications,” *Current Opinion in Neurobiology*, vol. 14, no. 5, pp. 610–616, 2004.
- [2] S. W. Hell and J. Wichmann, “Breaking the diffraction resolution limit by stimulated emission: stimulated-emission-depletion fluorescence microscopy,” *Opt. Lett.*, vol. 19, pp. 780–782, Jun 1994.
- [3] M. J. Rust, M. Bates, and X. Zhuang, “Sub-diffraction-limit imaging by stochastic optical reconstruction microscopy (storm),” *Nature Methods*, vol. 3, no. 10, pp. 793–796, 2006.
- [4] S. T. Hess, T. P. K. Girirajan, and M. D. Mason, “Ultra-high resolution imaging by fluorescence photoactivation localization microscopy,” *Biophysical Journal*, vol. 91, pp. 4258–4272, 2022/08/07 2006.
- [5] H. Kao and A. Verkman, “Tracking of single fluorescent particles in three dimensions: use of cylindrical optics to encode particle position,” *Biophysical Journal*, vol. 67, no. 3, pp. 1291–1300, 1994.
- [6] B. Huang, W. Wang, M. Bates, and X. Zhuang, “Three-dimensional super-resolution imaging by stochastic optical reconstruction microscopy,” *Science*, vol. 319, no. 5864, pp. 810–813, 2008.
- [7] S. Liu, E. B. Kromann, W. D. Krueger, J. Bewersdorf, and K. A. Lidke, “Three dimensional single molecule localization using a phase retrieved pupil function,” *Opt. Express*, vol. 21, pp. 29462–29487, Dec 2013.
- [8] S. Brasselet, “Polarization-resolved nonlinear microscopy: application to structural molecular and biological imaging,” *Adv. Opt. Photon.*, vol. 3, no. 3, p. 205, 2011.
- [9] J. Enderlein, E. Toprak, and P. R. Selvin, “Polarization effect on position accuracy of fluorophore localization,” *Opt. Express*, vol. 14, pp. 8111–8120, Sep 2006.
- [10] M. P. Backlund, M. D. Lew, A. S. Backer, S. J. Sahl, G. Grover, A. Agrawal, R. Piestun, and M. W. E., “Simultaneous, accurate measurement of the 3D position and orientation of single molecules,” *Proc. Nat. Acad. Sci.*, vol. 109, pp. 19087–92, 2012.
- [11] S. Stallinga and B. Rieger, “Position and orientation estimation of fixed dipole emitters using an effective hermite point spread function model,” *Opt. Express*, vol. 20, pp. 5896–5921, Mar 2012.
- [12] C. A. Valades Cruz, H. A. Shaban, A. Kress, N. Bertaux, S. Monneret, M. Mavrikis, J. Savatier, and S. Brasselet, “Quantitative nanoscale imaging of orientational order in biological filaments by polarized superresolution microscopy,” *Proceedings of the National Academy of Sciences*, vol. 113, no. 7, pp. E820–E828, 2016.
- [13] C. V. Rimoli, C. A. Valades-Cruz, V. Curcio, M. Mavrikis, and S. Brasselet, “4polar-storm polarized super-resolution imaging of actin filament organization in cells,” *Nat. Commun.*, vol. 13, no. 1, p. 301, 2022.
- [14] A. S. Backer, M. P. Backlund, A. R. von Diezmann, S. J. Sahl, and W. E. Moerner, “A bisected pupil for studying single-molecule orientational dynamics and its application to three-dimensional super-resolution microscopy,” *Applied Physics Letters*, vol. 104, no. 19, p. 193701, 2014.
- [15] O. Zhang, J. Lu, T. Ding, and M. D. Lew, “Imaging the three-dimensional orientation and rotational mobility of fluorescent emitters using the tri-spot point spread function,” *Applied Physics Letters*, vol. 113, no. 3, p. 031103, 2018.
- [16] V. Curcio, L. A. Alemán-Castañeda, T. G. Brown, S. Brasselet, and M. A. Alonso, “Birefringent fourier filtering for single molecule coordinate and height super-resolution imaging with dithering and orientation,” *Nat. Commun.*, vol. 11, no. 1, p. 5307, 2020.
- [17] C. N. Hulleman, R. Ø. Thorsen, E. Kim, C. Dekker, S. Stallinga, and B. Rieger, “Simultaneous orientation and 3d localization microscopy with a vortex point spread function,” *Nature Communications*, vol. 12, no. 1, p. 5934, 2021.

- [18] T. Ding and M. D. Lew, “Single-molecule localization microscopy of 3d orientation and anisotropic wobble using a polarized vortex point spread function,” *The Journal of Physical Chemistry B*, vol. 125, pp. 12718–12729, 11 2021.
- [19] T. Wu, J. Lu, and M. D. Lew, “Dipole-spread-function engineering for simultaneously measuring the 3d orientations and 3d positions of fluorescent molecules,” *Optica*, vol. 9, pp. 505–511, May 2022.
- [20] M. Böhmer and J. Enderlein, “Orientation imaging of single molecules by wide-field epifluorescence microscopy,” *J. Opt. Soc. Am. B*, vol. 20, pp. 554–559, Mar 2003.
- [21] M. A. Lieb, J. M. Zavislan, and L. Novotny, “Single-molecule orientations determined by direct emission pattern imaging,” *J. Opt. Soc. Am. B*, vol. 21, pp. 1210–1215, Jun 2004.
- [22] R. Luchowski, Z. Gryczynski, Z. Földes-Papp, A. Chang, J. Borejdo, P. Sarkar, and I. Gryczynski, “Polarized fluorescent nanospheres,” *Opt. Express*, vol. 18, pp. 4289–4299, Mar 2010.
- [23] L. Neumann, J. van Oever, and N. F. van Hulst, “A Resonant Scanning Dipole-Antenna Probe for Enhanced Nanoscale Imaging,” *Nano Letters*, vol. 13, pp. 5070–5074, Nov. 2013. Publisher: American Chemical Society.
- [24] K. Zhanghao, L. Chen, X.-S. Yang, M.-Y. Wang, Z.-L. Jing, H.-B. Han, M. Q. Zhang, D. Jin, J.-T. Gao, and P. Xi, “Super-resolution dipole orientation mapping via polarization demodulation,” *Light: Science & Applications*, vol. 5, pp. e16166–e16166, Oct. 2016.
- [25] P. N. Petrov, Y. Shechtman, and W. E. Moerner, “Measurement-based estimation of global pupil functions in 3d localization microscopy,” *Opt. Express*, vol. 25, pp. 7945–7959, Apr 2017.
- [26] Y. Li, Y.-L. Wu, P. Hoess, M. Mund, and J. Ries, “Depth-dependent psf calibration and aberration correction for 3d single-molecule localization,” *Biomed. Opt. Express*, vol. 10, pp. 2708–2718, Jun 2019.
- [27] T. Yan, C. J. Richardson, M. Zhang, and A. Gahlmann, “Computational correction of spatially variant optical aberrations in 3d single-molecule localization microscopy,” *Opt. Express*, vol. 27, pp. 12582–12599, Apr 2019.
- [28] B. Richards, E. Wolf, and D. Gabor, “Electromagnetic diffraction in optical systems, ii. structure of the image field in an aplanatic system,” *Proceedings of the Royal Society of London. Series A. Mathematical and Physical Sciences*, vol. 253, no. 1274, pp. 358–379, 1959.
- [29] E. Wolf, *Introduction to the theory of coherence and polarization*. Cambridge University Press, 2007.
- [30] L. Novotny and B. Hecht, *Principles of Nano-Optics*. Cambridge University Press, 2006.